applied sciences

MDPI

Article

Design of a Tubular Permanent Magnet Actuator for Active Lateral Secondary Suspension of a Railway Vehicle

Jun-Ho Yoon [1], Dongwook Kim [1], No-Cheol Park [1,*] and Young-Pil Park [2]

[1] Department of Mechanical Engineering, Yonsei University, Seoul 03722, Korea; junho@yonsei.ac.kr (J.-H.Y.); fromomega@naver.com (D.K.)
[2] Center for Information Storage Device, Yonsei University, Seoul 03722, Korea; park2814@yonsei.ac.kr
* Correspondence: pnch@yonsei.ac.kr; Tel.: +82-2-2123-4530

Academic Editor: Chien-Hung Liu
Received: 9 December 2016; Accepted: 4 February 2017; Published: 8 February 2017

Abstract: This paper describes the finite element (FE)-based design of a slotted tubular permanent magnet actuator (TPMA) used in railway vehicle active lateral secondary suspension that improves the actuator's thrust and lowers its cogging force under thermal and geometric constraints. To consider the electromagnetic and thermal fields and the complex interactions among the design variables, design was carried out in an electromagnet and thermal field environment using accurate and time-effective FE analysis. A six-slot prototype model was fabricated to estimate critical thermal parameters, which are difficult to compute without experiments. Three-dimensional FE analysis using the determined thermal parameters was adopted to calculate the precise thermal distribution of the TPMA and verify the forced air-cooling effect. A prototype TPMA with a quasi-Halbach array of permanent magnets and a moving magnet was manufactured through the FE-based design process; the dynamic, electromagnetic, and thermal characteristics of the prototype TPMA were validated experimentally.

Keywords: tubular permanent magnet actuator; active suspension; electromagnetic field analysis; heat transfer analysis

1. Introduction

With the increasing use of railway vehicles, many countries have become interested in the development of high-speed trains, as they have been proven to be an effective and economical means of transportation. However, increased train speeds cause significant vibration problems, which degrade passenger comfort and operational safety, and increase track maintenance costs [1,2]. Because modifications and improvements to railway vehicles to reduce vehicle vibration are less costly than modifications to the track, various types of suspension systems linking the bogies and the car bodies have been studied. One method, active lateral secondary suspension, has been developed to enhance or maintain passenger comfort in the face of increased vehicle speeds and inferior track conditions [3,4].

To apply active lateral secondary suspension, an actuator with high power density, high thrust force, and excellent servo characteristics must be installed between the car body and the bogie, to handle the heavy, floating weight of the car body and passengers. Over the last few decades, a variety of railway actuator types have been studied. Hydraulic actuators are compact and can easily be installed in the narrow spaces between the car body and the bogie [5,6]; however, they have a low control bandwidth and are at risk of oil leakage [7,8]. Furthermore, in order to control the force of hydraulic actuators, the hydraulic valve must be driven by an additional low-power electromagnetic actuator [9]. Moreover, a highly complex controller design is required to account for severe nonlinear

dynamics of hydraulic actuators [10–12]. Although pneumatic actuators are relatively cheap and there is no liquid leakage, the controllable frequency bandwidth is restricted to 2–3 Hz and they suffer from an air consumption problem [13,14]. Semi-active magnetorheological fluid damper can generate high yield strength, have low cost of production, require low power [15,16]. However, the force remains dependent upon the speed of damper movement, which means that large forces cannot be produced with low speed. Electromagnetic (EM) actuators exhibit good frequency response and allow for bidirectional power flow, thus enabling both active and passive modes [9,17–19]. In addition, EM actuators do not require continuous power, intricate control, or any fluid [20]. Among the various types of EM actuators, the tubular permanent magnet actuator (TPMA) is one of the most suitable actuators with all of the required characteristics [21–23].

Numerous studies have focused on a TPMA design to ensure maximum performance under constraints using electromagnetic and thermal analysis. Wang et al. [21] developed a high force density linear actuator for active vehicle suspension, which consists of a brushless tubular permanent-magnet actuator. A thermal network model has been established using the thermal resistances derived using the governing principle of heat conduction, assuming the thermal dissipation in the machine is predominant in the radial direction. The model was used to maximize thrust density against a given set of volumetric and thermal constraints. Although these methods provide analytical means for establishing a rough temperature distribution, they require a subsequent series of assumptions and experimental verification to obtain accurate results. In particular, several thermal parameters have a large effect on the temperature distribution of a TPMA, but it is difficult to obtain these data without experiments. Some of the data regard investigation of the interface gap between components, the forced convection heat transfer coefficient, the thermal conductivities of laminated stator cores, etc. [24]. Furthermore, since the cooling effect on the housing of the actuator is not considered during the design process, the temperature distribution of the final prototype with the housing may have a large error under forced convection conditions. Gysen et al. [25] developed an active electromagnet suspension system for automotive application by combining a brushless tubular permanent-magnet actuator with a passive spring. The target thrust force of the actuator was determined through a one-lap test drive. The performance of the actuator was analyzed for different magnetization topologies as well as for interior- and exterior-magnet solutions using the analytical method [26] for predicting electromagnetic performance and a two-dimensional (2-D) thermal finite element (FE) model. However, since the end effects of the finite length of the stator and translator are neglected in the above-mentioned electromagnetic analysis, it is difficult to accurately calculate the cogging force of the actuator. The cogging force of electromagnetic actuator is the force from the interaction between the permanent magnets of the mover and the stator slots. Since this force results in thrust ripples and reduces the servo characteristics, cogging force reduction is one of the most important factors to consider in the design of a permanent magnet actuator.

This paper describes an FE-based design of a slotted TPMA used for railway vehicle active lateral secondary suspension, which improves the actuator's thrust and lowers its cogging force under thermal and geometric constraints. The specifications of the TPMA were derived based on experimental data for a conventional passive damper used in a test train. A six-slot prototype model was constructed to determine and develop well-defined thermal parameters to ensure reliable thermal FE analysis. A three-dimensional (3-D) thermal FE analysis was adopted to calculate the precise thermal distribution of the TPMA and verify the forced air-cooling effect. According to various design variables, the change in electromagnetic and thermal characteristics were analyzed considering nonlinearity, forced air-cooling effects, and slot opening. Finally, a prototype TPMA was manufactured from the FE-based design, and the dynamic, electromagnetic, and thermal characteristics with forced air-cooling were verified experimentally.

2. Tubular Permanent Magnet Actuator (TPMA) Specifications

A schematic diagram of an active lateral secondary suspension system is shown in Figure 1. In the design, the electromechanical (EM) actuator is installed between the car body and the bogie. Using a spherical rubber joint consisting of a connecting rod and high-stiffness rubber, the stationary part of the actuator is connected to the bogie, and the moving part is connected to the interface bolster under the car body. Two EM actuators are installed at each end of the car body.

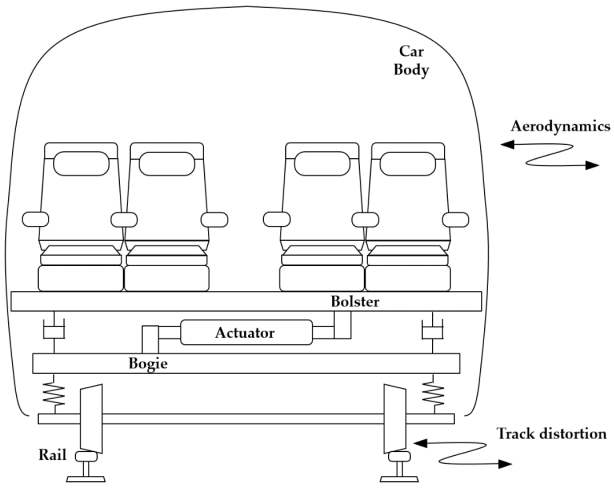

Figure 1. Schematic diagram of active lateral secondary suspension.

The size, bandwidth, thrust, stroke, and allowable temperature make up the specifications of the TPMA for active lateral secondary suspension. These specifications must be clearly defined to utilize the active lateral secondary suspension effectively. The size specifications were determined by considering the size of the prototype test bogie and bolster to be developed for the railway vehicle with active lateral secondary suspension. The stator outer diameter and axial length were set to 200 mm and 1000 mm, respectively, by considering the available space between the bogie and the interface bolster where the TPMAs were installed, as shown in Figure 1.

In a railway vehicle, the ride comfort of passengers is decreased by vibration disturbances. There are two different methods that can be used to evaluate the effect of active lateral secondary suspension: Wz and ISO [3,27]. In the Wz method, 3–7 Hz is the sensitive range for lateral vibration, and the 0.6–2 Hz component of lateral vibration has a large influence on ride comfort in the case of ISO 2631 [28].

To reduce the lateral vibration of a railway car, a high thrust force is required to move the car body, which weighs dozens of tons, and a low cogging ripple is necessary to provide excellent servo characteristics. The design must achieve the thrust goal under conditions that do not exceed the allowable temperature, and a sufficient axial stroke must be ensured to avoid failure of the railway vehicle and actuator due to sudden shocks. When traveling around a curve with a small radius at high speed, the car body tends to move laterally outward in relation to the track and bogies; thus, a quasi-static displacement arises between the stationary part connected to the bogie and the moving part connected to the car body due to centrifugal force; the moving part may collide with the stationary part, which could ultimately lead to actuator failure.

To determine the target thrust force and stroke, driving tests were performed using a test train with conventional lateral passive dampers. In order to measure the behavior of the convectional passive damper, a non-contact laser sensor was installed between the car body and bogie. The relative velocity and displacement between the damper and the car body were measured. Figure 2 shows the relative lateral velocity and displacement distributions of the front and rear conventional lateral passive dampers. In real track experiments where the maximum speed of the test train was 210 km/h,

the lateral relative velocities were generally less than 0.05 m/s, and the relative displacements were generally less than 10 mm. However, the maximum displacement was 40 mm and the maximum velocity was 0.22 m/s. According to the real track experimental results, the stroke of the TPMA must be greater than ±40 mm. Thus, the stroke of the TPMA was set to ±50 mm. The maximum target thrust force was 7700 N, calculated by considering the measured maximum velocity and the damping coefficient of the passive damper, which was 35 kNs/m.

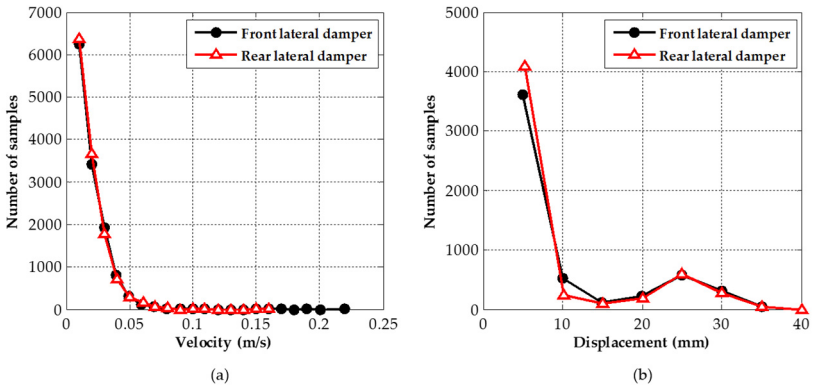

Figure 2. Real track experimental results with conventional lateral passive dampers: (**a**) relative lateral velocity; (**b**) relative displacement.

As the operating temperature of the electromagnetic actuator increases, the life of the insulator decreases. If the actuator constantly operates above the maximum allowable temperature, it causes a thermal problem and the actuator will not operate [29]. As this is an important factor that prevents damage to the insulating material, the maximum allowable temperature of the actuator was determined by considering the insulation of the component. The maximum allowable temperature of the TPMA is 130 °C, corresponding to insulation class B. Because these criteria are related to the thermal characteristics and the target thrust of the actuator, they must always be considered in the design process. The TPMA specifications for active lateral secondary suspension of a railway vehicle are summarized in Table 1.

Table 1. Specifications of the tubular permanent magnet actuator.

Specification	Value
Stator outer diameter	0.200 m
Axial length	1.000 m
Bandwidth	10 Hz
Stroke	±0.050 m
Maximum thrust force	7700 N
Allowable maximum temperature	130 °C
Maximum current limit	100 A

3. Electromagnetic and Thermal Finite Element (FE) Model

3.1. Overall Structure

In order to apply an active lateral suspension system to a railway vehicle under the aforementioned design constraints, it is important to choose an appropriate topology from among the various geometric arrangements available for the TPMA design, as shown in Figure 3. In a tubular machine, there are two main components: the moving element (referred as the mover) and the stationary element (referred as the stator). The overall configuration is classified as either a 'moving magnet' or a 'moving coil.' In a moving magnet configuration, magnets are placed on the mover and coils are placed on the stator.

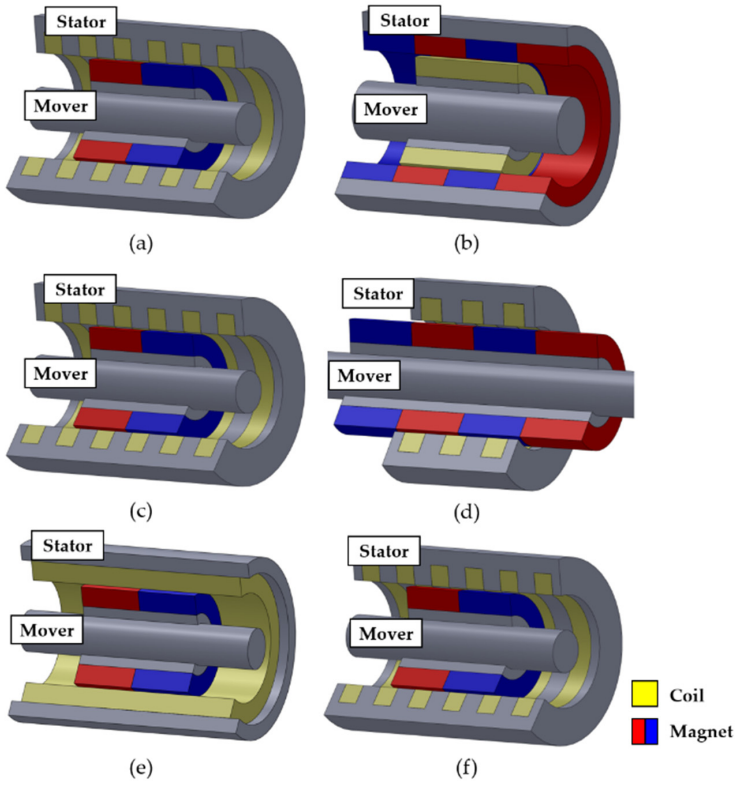

Figure 3. Various tubular configurations: (**a**) moving magnet; (**b**) moving coil; (**c**) short mover; (**d**) long mover; (**e**) slotless; (**f**) slotted.

In an active lateral secondary suspension, a moving magnet configuration is more suitable than a moving coil configuration since its interior magnet topology eliminates the cable slab and its thermal characteristics are excellent because the exterior coils (which are primary heat sources) effectively expel the heat.

For comparable sizes and weights, the force density attainable by a long tubular mover arrangement is higher than that attainable by a short tubular mover arrangement. However, a short tubular mover arrangement is more appropriate for this application because of the large stroke of the TPMA in the limited design space.

In addition, tubular topologies considering the core shape are divided into slotless and slotted types. A slotted actuator has a large cogging ripple compared to a slotless actuator, but a slotted actuator can generate higher thrust forces because of the magnetic field generated by the interaction between the magnets and the core. Also, the cogging force of a slotted actuator can be sufficiently reduced by design optimization.

Figure 4 shows the overall structure of the TPMA. The mover consisted of segmented magnets, a yoke, and a shaft. The stator consisted of five pairs of three-phase U, V, and W coils, a laminated core, and an aluminum housing that contained the cooling fin. Laser displacement sensors were used to measure the axial position of the mover. Figure 5 shows the topology and the design variables of the TPMA. The initial design variables of the TPMA are summarized in Table 2.

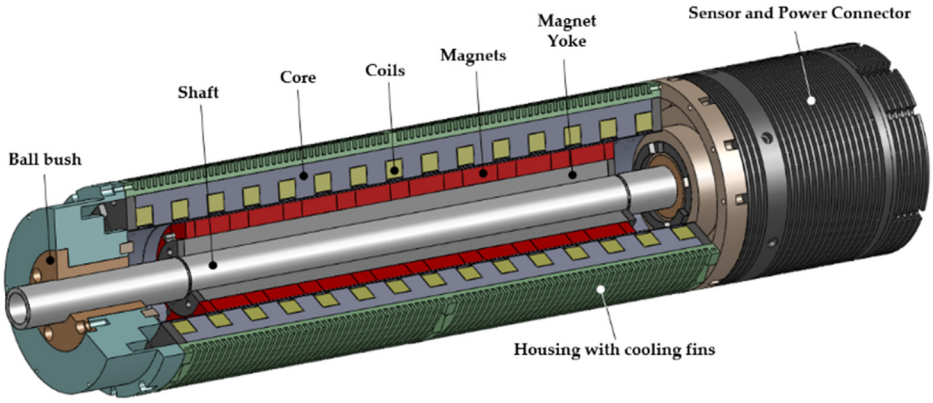

Figure 4. Overall structure of the tubular permanent magnet actuator for the active lateral secondary suspension.

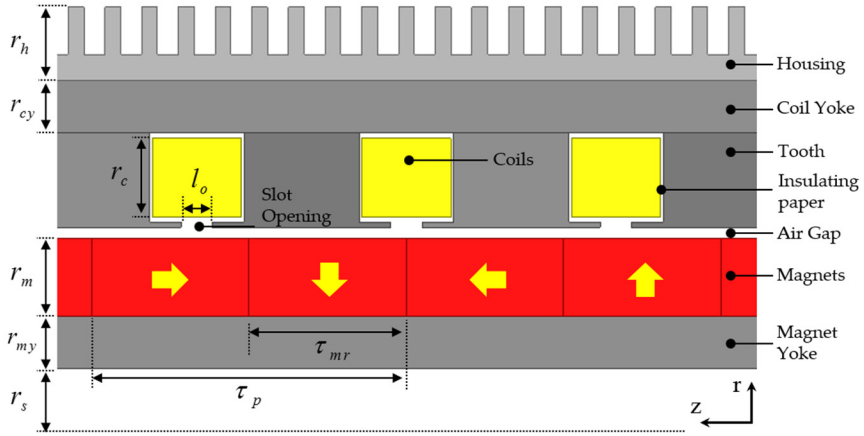

Figure 5. Topology and design variables of the tubular permanent magnet actuator (axial cross-section).

Table 2. Initial and fixed design variables of the tubular permanent magnet actuator.

Initial Design Variables	Value	Fixed Variables	Value
Height of coil yoke r_{cy}	10 mm	Height of housing r_h	14 mm
Height of coil r_c	15 mm	Radius of shaft r_s	15 mm
Height of magnet r_m	15 mm	Pole-pitch	60 mm
Height of magnet yoke r_{my}	10 mm	Air gap l_g	2 mm
τ_{mr} to τ_p ratio	0.5	Thickness of insulating paper l_p	0.5 mm
Slot opening l_o	6 mm	Number of pole-pairs	4
-	-	Number of slots	15

3.2. Thermal Model Parameters

Although some thermal variables such as thermal contact resistance, the interface gap between components, and the forced convection heat transfer coefficient have a large effect on the temperature distribution of the TPMA, they are difficult to calculate without experiments or working experience of similar designs [24]. Thus, a six-slot prototype model, shown in Figure 6a, was fabricated to estimate the critical thermal parameters of the TPMA with initial and fixed design variables, as shown in Table 2. The six-slot prototype consisted of two pairs of three-phase coils, a laminated core, and an aluminum housing with fins. The air-cooling system was composed of annular fins circumferentially attached to the cylinder, and designed to enhance heat transfer from the surface to the surrounding air. The fin was designed in consideration of the manufacturing limitations, allowable stiffness, and cooling

efficiency. The temperatures of eight points (on the outer surface of the mover, coils, and housing, and on the inner surface of the cores) were measured using thermocouples.

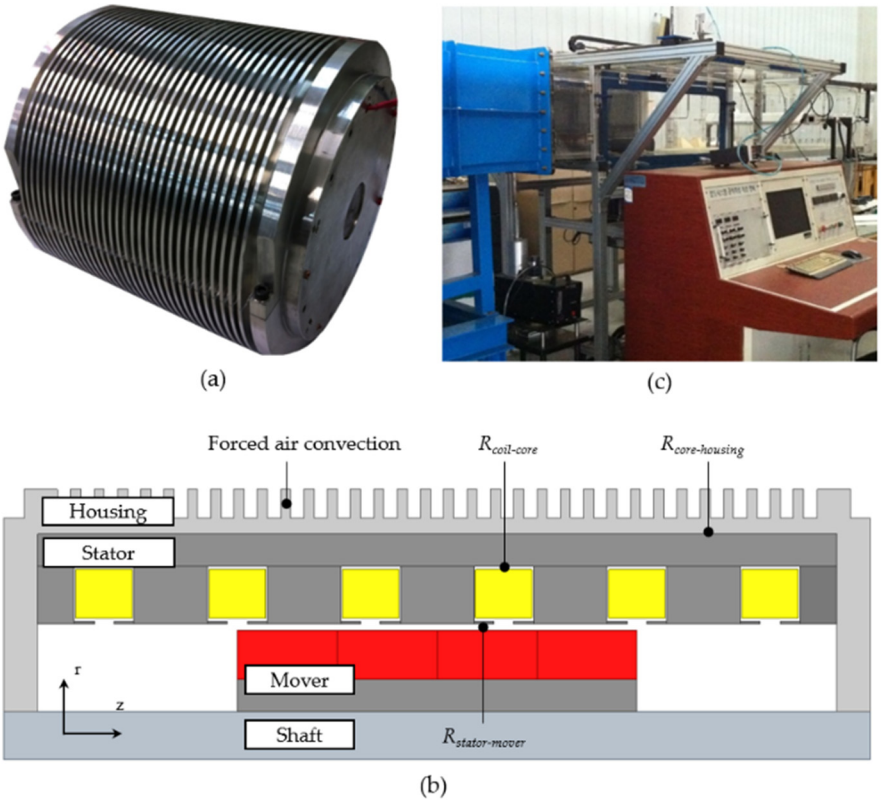

Figure 6. Six-slot prototype model: (**a**) manufactured six-slot prototype; (**b**) critical thermal parameters; (**c**) wind tunnel test.

There are five critical thermal parameters that can affect the thermal characteristics: the thermal contact resistance between the coil and the core, the core and the housing, and the stator and the mover; the thermal conductivity of the laminated core; and the coefficient of forced convection of the housing with fins, shown in Figure 6b. In general, it is difficult to estimate the air flow through a TPMA under a car body when the train is in motion. Therefore, to propose design guidelines for the air-cooling system, the flow through the TPMA must be simplified, and the cooling effect with respect to the air velocity must be verified experimentally. Figure 6c shows the setup for a wind-tunnel test of the six-slot prototype model. The external air flow in the direction normal to the axis of the TPMA and the thermal characteristics were validated from low to high speed (30 m/s). The thermal analysis was performed using 3-D FE analysis to ensure accurate simulation results [30]. Accordingly, to increase the reliability of the thermal FE model, the thermal experiments were carried out at three input direct current (DC) continuously induced in the three-phase coils.

Figure 7a shows the results of the wind tunnel test at various air velocities. The maximum temperature in the coil decreased exponentially with air velocity. It was confirmed that air velocities from 3 m/s to 10 m/s substantially affected the thermal performance but enhancement of air cooling was markedly diminished at air velocities higher than 10 m/s. The coefficients of forced convection of the heat sink were determined for each wind speed. The measured temperature distributions agreed well with FE analysis using the determined thermal parameters, as shown in Figure 7b. Thus, the reliability of the five parameters was verified. The thermal properties used in the simulation are summarized in Table 3.

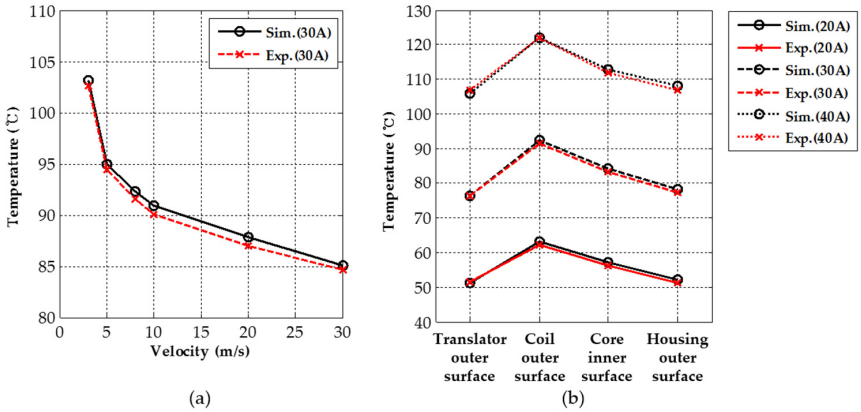

Figure 7. Saturation temperature of six-slot prototype model: (**a**) maximum temperature of the coil at various air velocities with a direct current of 30 A; (**b**) temperature distribution at three input currents with 8 m/s forced convection.

Table 3. Thermal properties for thermal simulation.

Material	Conductivity (W/m-k)	Specific Heat (J/kg-k)	Density (kg/m^3)
Air	0.0263	1007	1.1614
Copper	400.0	385.0	8933
Silicon Steel	24.2 (r direction) 5.0 (z direction)	446.0	7650
Aluminum	210.0	900.0	2700
NdFeB	6.5	460.0	7600
$R_{coil\ to\ core}$	0.1	-	-
$R_{stator\ to\ mover}$	0.15	-	-
$R_{core\ to\ housing}$	0.3	-	-

3.3. Electromagnetic and Thermal Modelling of TPMA

Both electromagnetic and thermal analyses are essential when designing a TPMA, because the thermal and electromagnetic characteristics are coupled [31]. Thus, a coupled-fields analysis model was applied. The results of the EM analysis were used as heat sources for the thermal analysis, and the results of the thermal analysis were then used to describe changes in the EM field caused by the heat source.

Electromagnetic FE techniques provide an accurate means of determining the field distribution, including cases with flux leakage, fringing, magnetic saturation, and complex core shapes [32]. The EM analysis was performed using an FE model considering nonlinear magnetic and cylindrical symmetric conditions. A 3-D FE analysis is required to calculate the eddy current loss from permanent magnets accurately [33]. However, in the case of the proposed TPMA, the eddy current loss was as small as 0.25% of the copper loss because the servo bandwidth of the TPMA was 10 Hz and the core of the stator was composed of laminated silicon steel. Accordingly, time-effective two-dimensional (2-D) FE analysis was used for the design; the accuracy of the 2-D FE model was verified by comparison with the results of the 3-D FE model. The difference between the magnetic flux density in the air gap was less than 1%.

The 2-D cylindrical FE model consisted of five pairs of three-phase coils, a laminated silicon steel core, and quasi-Halbach magnets. The aluminum housing and austenitic stainless steel shaft were excluded from the model because they do not affect the magnetic fields. Figure 8a shows the FE-predicted open-circuit flux distributions for zero axial displacements using the commercial software ANSYS Maxwell (V17.2.0, Ansys, Inc., Canonsburg, PA, USA). The TPMA thermal analysis model was built in three dimensions and applied to the boundary conditions and thermal critical parameters throughout the previous six-slot prototype experiment to find the temperature increase

and the maximum temperature due to losses from each part of the actuator. As shown in Figure 8b, the 3-D thermal FE model consisted of five pairs of three-phase coils, a laminated core, an aluminum cover, a magnet, a yoke, a shaft, and a housing. A one-sixth cylindrical model was used to reduce the analysis time. The maximum saturated temperature was 112 °C in the V phase coil with DC 80 A and 3 m/s forced convection using the commercial software ANSYS (V17.2.0, Ansys, Inc., Canonsburg, PA, USA); heat was transferred through conduction and convection.

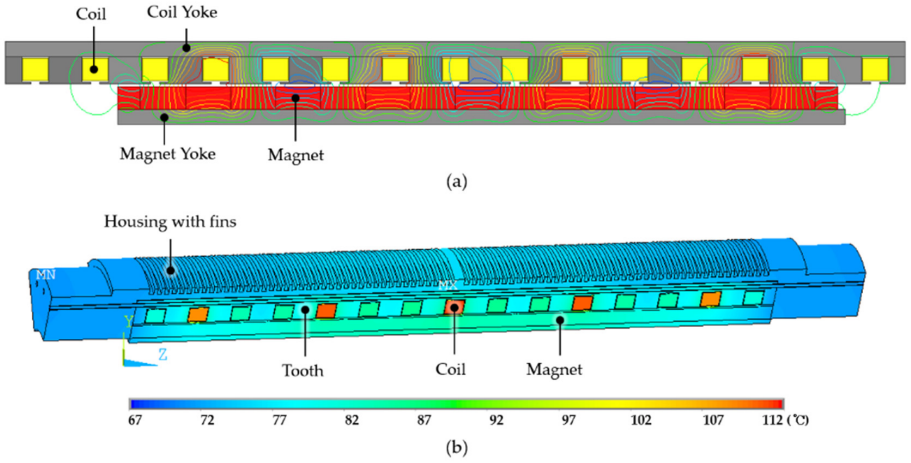

Figure 8. Finite element (FE) model of the tubular permanent magnet actuator: (**a**) open-circuit flux distributions of the electromagnetic two-dimensional FE model; (**b**) temperature distribution with DC 80 A and 3 m/s forced convection.

4. Performance Analysis and Design of the TPMA

Figure 9 shows the design procedure of the TPMA. The gradient-based optimization method was used to maximize the thrust density and minimize the cogging force under the geometric and thermal constraints. The thrust density, maximum cogging force, and losses were determined by electromagnetic 2-D FE analysis of the initial models. The maximum cogging force was obtained by calculating the cogging force at each axial position without current. The temperature distribution was determined by thermal 3-D FE analysis considering forced convection using the thermal parameters determined through thermal experiments. Table 4 lists the design specifications, including the peak temperature, geometrical limitations, and design domains.

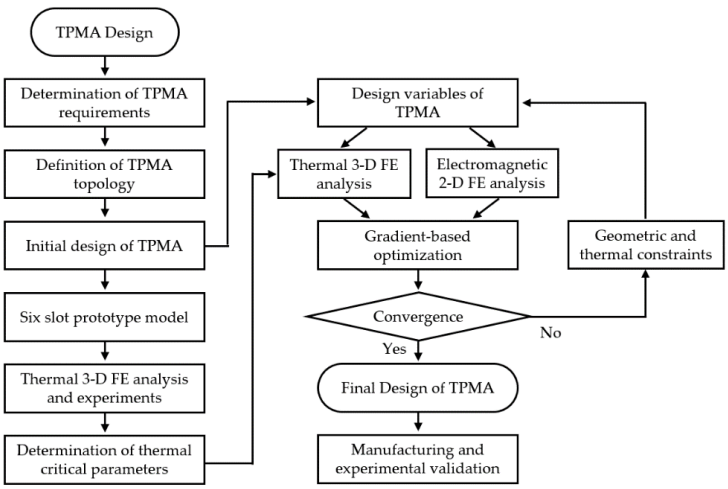

Figure 9. Design procedure of the tubular permanent magnet actuator for the active lateral secondary suspension of a railway vehicle.

Table 4. Design constraints and other data.

Type	Values
Thermal constraints	Maximum temperature $T_p \leq 130$
Geometric constraints	Stator outer radius $R_o \leq 100$ (mm)
Design domain	$R_1 = \{r_{my} \mid 4 < r_{my} < 7\}$ $R_2 = \{r_m \mid 12 < r_m < 18\}$ $R_3 = \{r_c \mid 13 < r_c < 20\}$ $R_4 = \{r_{cy} \mid 7 < r_{cy} < 13\}$ $Z_1 = \{\tau_{mr}/\tau_p \mid 0.5 < \tau_{mr}/\tau_p < 0.75\}$ $Z_2 = \{l_o \mid 2 < l_o < 16\}$
Other data	Current density J = 7.36 (A/mm^2) Forced convection coefficient 38 (W/m^{2}K) [1]

[1] at 8 m/s forced convection.

Figures 10 and 11 show the thrust density and the maximum temperature variation with radial variables using the electromagnetic and thermal FE analysis. To analyze the effect of each radial design variable on the thrust density and the maximum temperature, variables such as air gap, height of housing, radius of shaft and thickness of insulating paper were fixed. Although increasing the number of turns is the easiest technique for improving the thrust density, it engenders thermal complications, as shown in Figures 10d and 11d. When the height of the coil is larger than 17 mm, the thrust density becomes higher than 3.363 $\times$ 10^5 N/m^3, but the maximum temperature of the actuator becomes higher than the allowable temperature. For this reason, the magnetic flux density must be improved to maximize the thrust force. However, at high magnetic flux densities, hysteresis and magnetic saturation effects occur in magnetic substances such as silicon steel [34].

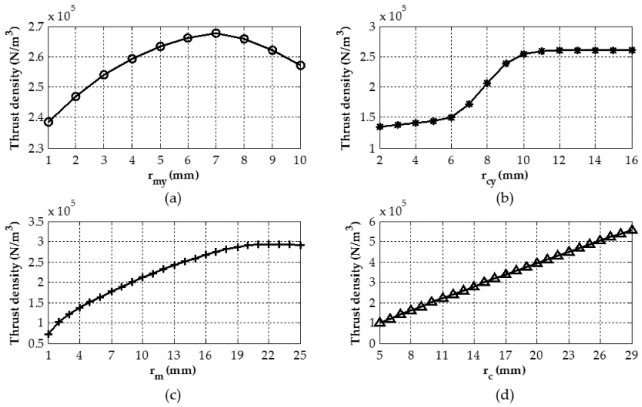

Figure 10. Thrust density versus the radial variables: (**a**) magnet yoke; (**b**) coil yoke; (**c**) magnet; (**d**) coil.

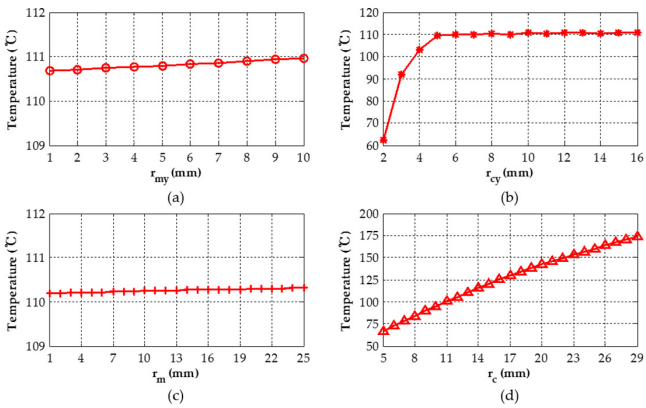

Figure 11. Maximum temperature versus the radial variables: (**a**) magnet yoke; (**b**) coil yoke; (**c**) magnet; (**d**) coil.

The heat generated in the coil is mainly transferred to the housing through the tooth and coil yoke, and the amount transferred to the mover is small due to the low thermal conductivity of the air. For this reason, the change in height of the magnet yoke and magnet does not significantly affect the maximum temperature of the actuator as shown in Figure 11a,c. However, as the magnet height increases, the magnetic flux density increases and the thrust density increases until magnetic saturation occurs as shown in Figure 10c. Figure 10a shows that there is an optimal magnet yoke height value to maximize the thrust density. As the height of the coil yoke becomes smaller than a certain value, the cooling effect by the forced convection is greatly improved, but at the cost of a reduced thrust density, as shown in Figures 10b and 11b.

A Halbach array is a special arrangement of permanent magnets that augments the magnetic field on one side of the array while cancelling the field to near zero on the other side. It has a number of attractive characteristics, including a sinusoidal back-electromotive-force waveform, a high force capability, and a low cogging force [35,36]. Because it is relatively difficult to manufacture magnets with an ideal Halbach magnetization, a simpler form, referred to as a quasi-Halbach magnetization, is preferred [35].

When the mover is in the initial center position, the net cogging force is zero because the permanent magnet is aligned with the stator teeth. However, when the mover has moved to the axial position in which the magnet flux is not in alignment with stator teeth, the net cogging force is no longer zero [37]. Figure 12 shows the variation of the maximum cogging force with respect to the quasi-Halbach ratio and slot opening. According to these two axial design variables, the magnetic flux density at the teeth changes, and the maximum cogging force value changes accordingly. As shown in Figure 12a, when the ratio shifted from 0.5 to 0.6 at 8 mm slot opening, the maximum cogging force decreased from 1575 to 223 N. And when the slot opening decreased from 16 to 6 mm at 0.6 ratio, the maximum cogging force reduced from 952 to 162 N. Therefore, there are optimal values of axial variables that minimize the cogging force. Figure 12a–c shows that although the coil height increases from 10 to 20 mm, there is almost no change in the optimum value of axial variables. However, the optimum value changes depending on the height of the magnet which directly affects the magnetic flux density, as shown in Figure 12d–f.

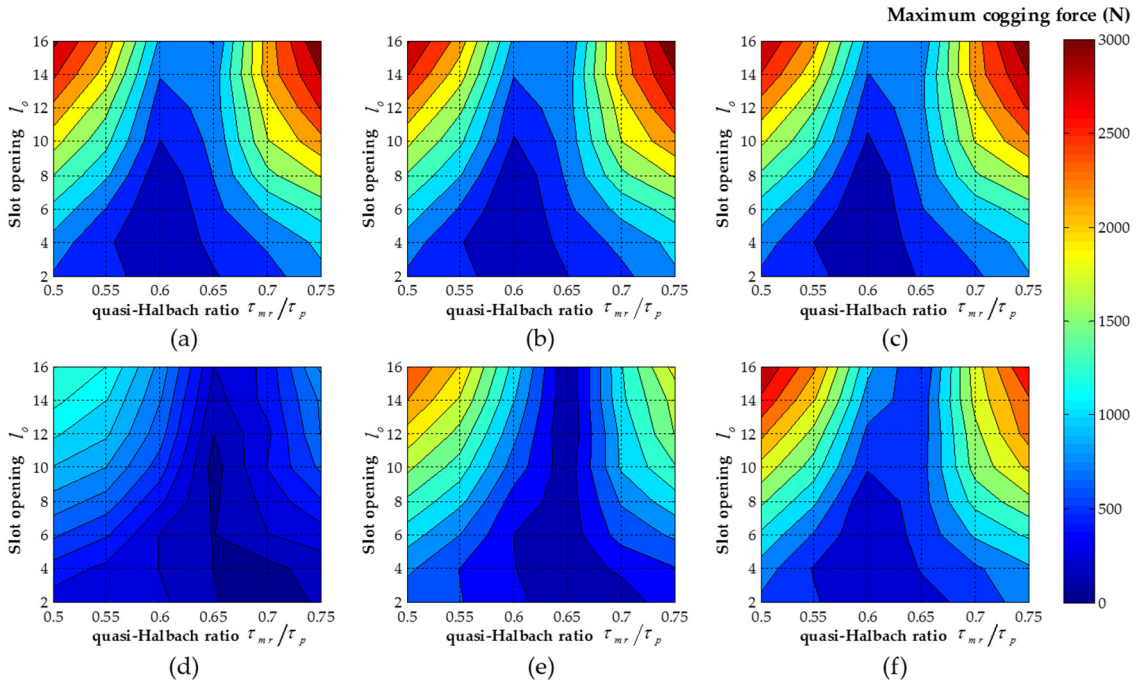

Figure 12. Maximum cogging force versus axial variables: (**a**) r_c = 10 mm; (**b**) r_c = 15 mm ; (**c**) r_c = 20 mm ; (**d**) r_m = 5 mm ; (**e**) r_m = 10 mm ; (**f**) r_m = 15 mm.

Gradient-based optimization was used to maximize the thrust density and minimize the cogging force under the geometric and thermal constraints and systematically modify the design variables in the model. The established problem is of a multi-objective optimization and the weighted-sum approach technique is applied to solve it [38]. The objective function was the sum of the reciprocal average thrust density and the maximum cogging force to find a unique objective function. Through optimization, the thrust density (force per unit volume) of the initial model increased by 35% from 2.252×10^5 to 3.120×10^5 N/m^3 under the thermal constraints, and the maximum cogging force decreased by 89% from 2216 to 220 N, which is a reasonable value that is less than 3% of the target thrust force. Table 5 lists the optimized design variables.

Table 5. Initial and optimized design variables.

Variables	Initial	Optimized
Stator outer radius R_o	100 mm	100 mm
Height of housing r_h	14 mm	14 mm
Height of coil yoke r_{cy}	10 mm	12 mm
Height of coil r_c	15 mm	17 mm
Air gap l_g	2 mm	2 mm
Height of magnet r_m	15 mm	16 mm
Height of magnet yoke r_{my}	10 mm	6 mm
τ_{mr} to τ_p ratio	0.5	0.64
Slot opening l_o	6 mm	13.4 mm
Radius of shaft r_s	15 mm	15 mm
Pole-pitch τ_p	60 mm	60 mm
Thickness of insulating paper l_p	0.5 mm	0.5 mm
Number of pole-pairs	4	4
Number of slots	15	15
Current density J	7.36 A/mm^2	7.36 A/mm^2
Winding turns N	117	133
Saturation temperature	93 °C	130 °C
Thrust density	2.252×10^5 N/m^3	3.120×10^5 N/m^3
Maximum cogging force	2216 N	220 N
Thrust ripple	28.8%	2.86%

5. Experimental Verification

Figure 13 shows the manufactured TPMA and the experimental setup. The TPMA was fabricated using the previously determined design variables. The axial length and outer diameter of the TPMA were 1 m and 200 mm, respectively, and its weight was 108 kg. A ball screw motor (APM-SE11MC(G7)K1, Mecapion Co., Ltd., Daegu, Korea), connected in series with a load cell (LS-2, CAS Co., Ltd., Jeongeup, Korea) and the shaft of the mover, was installed to measure the cogging force and the thrust force. The data acquisition system was configured to obtain temperature data from the thermocouples embedded in the TPMA.

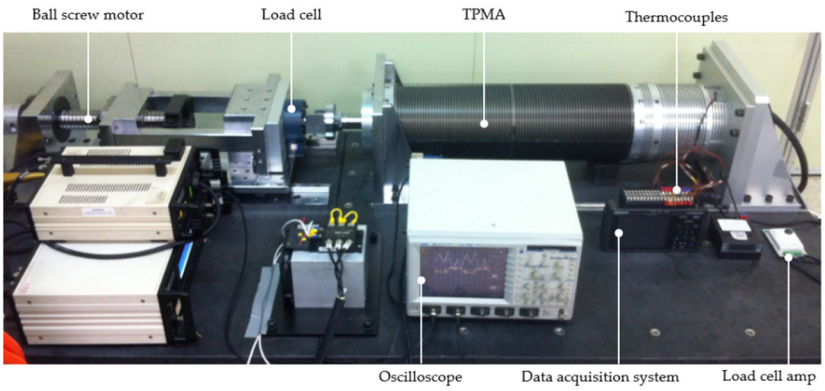

Figure 13. Experimental setup of the tubular permanent magnet actuator.

The thrust force was measured while increasing the current to a locked TPMA. As shown in Figure 14a, the measured thrust force increased linearly with the input current in both the positive and negative directions. The thrust force was 7700 N when the input current reached 96.3 A, and there was no saturation up to 102 A.

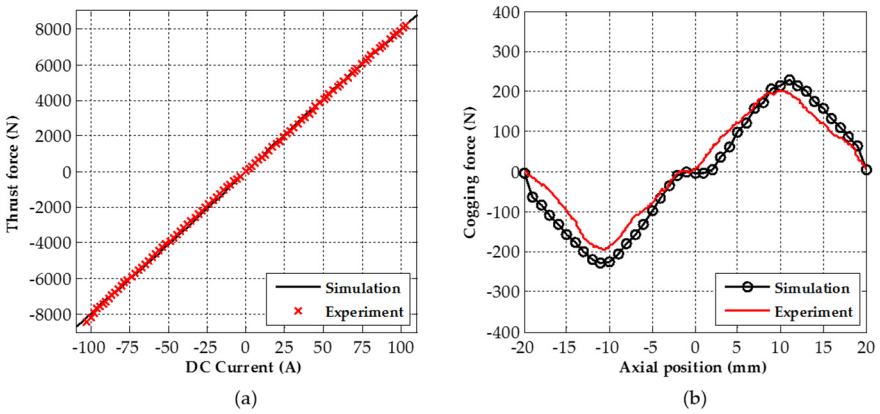

Figure 14. Force characteristics of tubular permanent magnet actuator: (**a**) thrust; (**b**) cogging.

The cogging force for a 40 mm period was measured while the mover slowly shifted using the ball screw motor. As shown in Figure 14b, the experimental results matched the simulation results well. The maximum cogging force was low compared with the maximum thrust force. Moreover, as the cogging force was constant at a given position, cogging force ripples could be compensated for via a feedforward control algorithm. The frequency response in Figure 15 shows that the bandwidth of the TPMA was greater than 10 Hz. Because the resonant frequency of the experimental setup was 24 Hz, the thrust constant increased by 6.3%. A phase shift of -7° was caused by hysteresis of the load cell. Furthermore, a phase delay at frequencies above 10 Hz is related to the current amplifier dynamic.

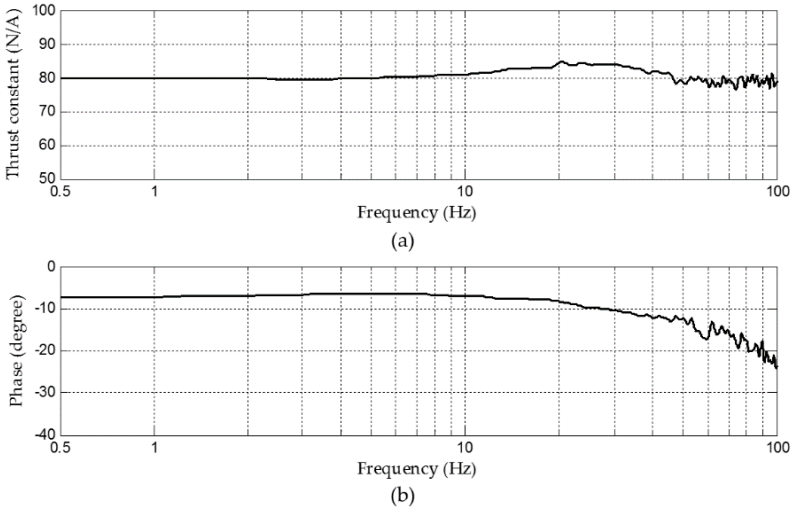

Figure 15. Frequency response function of the tubular permanent magnet actuator: (**a**) thrust constant; (**b**) phase.

To measure the temperature of each component, the thermocouples were imbedded in the TPMA. Other thermocouples were used to measure the ambient and housing outer surface temperatures. Figure 16a shows the experimental results for an input current of 96.3 A, corresponding to 7700 N. The current was applied for at least 1 h and the maximum temperature was 130 °C. Convergence was

achieved with a wind speed of 8 m/s at ambient temperature. This speed can be achieved using flow ducts without an additional cooling fan due to the high speed of the railway. As shown in Figure 16b, since well-defined thermal parameters were applied to the thermal FE model, the error between the experiment and the analysis was small, about 1.5%.

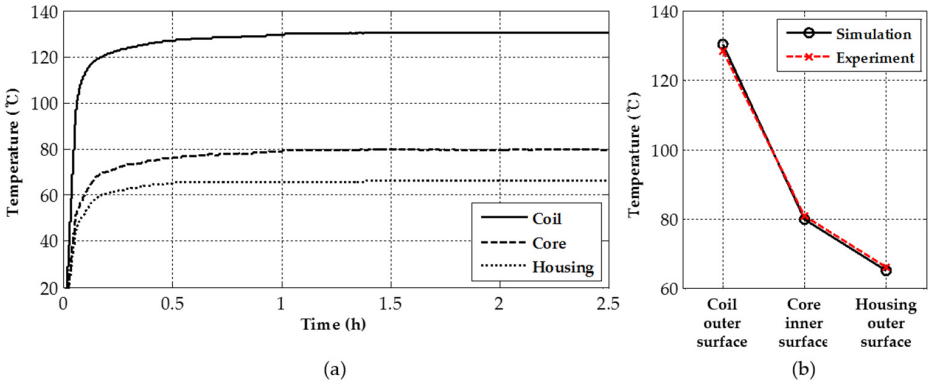

Figure 16. Thermal experimental results for the tubular permanent magnet actuator with 96.3 A and 8 m/s forced convection: (**a**) temperature rise of the TPMA with time; (**b**) saturation temperature.

Thermal experiments were performed to ensure robust thermal characteristics under harsh environmental conditions. Here, the phrase 'harsh environmental conditions' refers to continued operation until the temperature is saturated. In other words, the TPMA was designed conservatively. In reality, the TPMA operates at the maximum thrust force for only a few seconds and the temperature of the coil does not reach the allowable maximum [39]. Thus, for a high-speed railway, the TPMA can operate normally, even when the outside temperature is high.

6. Conclusions

The design of a three-phase slotted tubular permanent magnet actuator (TPMA) with quasi-Halbach magnetization for improved thrust and reduced cogging force was introduced in this paper. The design was conducted using accurate and time-effective finite element (FE) analysis. Critical thermal parameters were determined through experiments on a six-slot prototype model. Through FE-based optimization, the thrust density increased by 35% considering magnetic saturation and forced convection under thermal and geometric constraints, and the cogging force of the prototype was reduced by 89% considering the quasi-Halbach array and slot opening. The thermal and dynamic characteristics of the prototype TPMA were verified by simulation and experiment. The results presented in this paper demonstrate that the proposed electromagnetic and thermal FE analysis can be used to verify the dynamic, electromagnetic, and thermal characteristics of an electromagnetic actuator. The proposed design contributes to the design of a large-scale tubular electromagnetic actuator, which can be applied to active lateral secondary suspension of a railway vehicle.

Acknowledgments: This work was supported by the National Research Foundation of Korea (NRF) Grant funded by the Korean Government (MSIP) (No. 2015R1A5A1037668).

Author Contributions: J.-H.Y. contributed to the overall study, developed the methodology, built the FE model, performed simulations and experiments, analyzed data, and wrote the paper. N.-C.P. and Y.-P.P. supervised the work, edited the manuscript, and provided valuable suggestions to improve this paper. D.K. helped to build the prototype, assisted to build the thermal FE model.

Conflicts of Interest: The authors declare no conflict of interest.

References

1. Kaloop, M.R.; Hu, J.W.; Elbeltagi, E. Evaluation of high-speed railway bridges based on a nondestructive monitoring system. *Appl. Sci.* **2016**, *6*, 24. [CrossRef]

2. Lee, C.-M.; Goverdovskiy, V.; Sim, C.-S.; Lee, J.-H. Ride comfort of a high-speed train through the structural upgrade of a bogie suspension. *J. Sound Vib.* **2016**, *361*, 99–107. [CrossRef]
3. Orvnäs, A.; Stichel, S.; Persson, R. Ride comfort improvements in a high-speed train with active secondary suspension. *J. Mech. Syst. Transp. Logist.* **2010**, *3*, 206–215. [CrossRef]
4. Wang, P.; Li, H.; Zhang, J.; Mei, T. An analytical design approach for self-powered active lateral secondary suspensions for railway vehicles. *Veh. Syst. Dyn.* **2015**, *53*, 1439–1454. [CrossRef]
5. Foo, E.; Goodall, R. Active suspension control of flexible-bodied railway vehicles using electro-hydraulic and electro-magnetic actuators. *Control Eng. Pract.* **2000**, *8*, 507–518. [CrossRef]
6. Goodall, R.; Freudenthaler, G.; Dixon, R. Hydraulic actuation technology for full-and semi-active railway suspensions. *Veh. Syst. Dyn.* **2014**, *52*, 1642–1657. [CrossRef]
7. Goodall, R.; Pearson, J.; Pratt, I. Actuator Technologies for Secondary Active Suspension on Railway Vehicles. In Proceedings of the International Conference on Speedup Technology for Railway and Maglev Vehicles, Yokohama, Japan, 22–26 November 1993; 1993.
8. Karimi, H.R. Optimal vibration control of vehicle engine-body system using haar functions. *Int. J. Control Autom. Syst.* **2006**, *4*, 714.
9. Martins, I.; Esteves, J.; Marques, G.D.; da Silva, F.P. Permanent-magnets linear actuators applicability in automobile active suspensions. *IEEE Trans. Veh. Technol.* **2006**, *55*, 86–94. [CrossRef]
10. Li, H.; Jing, X.; Karimi, H.R. Output-feedback-based h∞ control for vehicle suspension systems with control delay. *IEEE Trans. Ind. Electron.* **2014**, *61*, 436–446. [CrossRef]
11. Bououden, S.; Chadli, M.; Karimi, H.R. A robust predictive control design for nonlinear active suspension systems. *Asian J. Control* **2016**, *18*, 122–132. [CrossRef]
12. Rath, J.J.; Defoort, M.; Karimi, H.R.; Veluvolu, K.C. Output feedback active suspension control with higher order terminal sliding mode. *IEEE Trans. Ind. Electron.* **2016**, *64*, 1392–1403. [CrossRef]
13. Norinao, H. Active and semi-active suspensions smooth 300 km/h ride. *Railw. Gaz. Int.* **1997**, 241–242.
14. Mellado, A.C.; Casanueva, C.; Vinolas, J.; Giménez, J.G. A lateral active suspension for conventional railway bogies. *Veh. Syst. Dyn.* **2009**, *47*, 1–14. [CrossRef]
15. Zapateiro, M.; Luo, N.; Karimi, H.; Vehi, J. Vibration control of a class of semiactive suspension system using neural network and backstepping techniques. *Mech. Syst. Signal Process.* **2009**, *23*, 1946–1953. [CrossRef]
16. Zapateiro, M.; Pozo, F.; Karimi, H.R.; Luo, N. Semiactive control methodologies for suspension control with magnetorheological dampers. *IEEE/ASME Trans. Mechatron.* **2012**, *17*, 370–380. [CrossRef]
17. Pollard, M.; Simons, N. Passenger comfort—the role of active suspensions. *Proc. Inst. Mech. Eng. D J. Automob. Eng.* **1984**, *198*, 161–175. [CrossRef]
18. Ribeiro, R.; Asadi, E.; Khamesee, M.B.; Khajepour, A. Hybrid variable damping control: Design, simulation, and optimization. *Microsyst. Technol.* **2014**, *20*, 1723–1732. [CrossRef]
19. Asadi, E.; Ribeiro, R.; Khamesee, M.B.; Khajepour, A. Analysis, prototyping and experimental characterization of an adaptive hybrid-electromagnetic damper for automotive suspension systems. *IEEE Trans. Veh. Technol.* **2016**. [CrossRef]
20. Gysen, B.L.; Paulides, J.J.; Janssen, J.L.; Lomonova, E.A. Active electromagnetic suspension system for improved vehicle dynamics. *IEEE Trans. Veh. Technol.* **2010**, *59*, 1156–1163. [CrossRef]
21. Wang, J.; Wang, W.; Atallah, K. A linear permanent-magnet motor for active vehicle suspension. *IEEE Trans. Veh. Technol.* **2011**, *60*, 55–63. [CrossRef]
22. Gysen, B.L.; van der Sande, T.P.; Paulides, J.J.; Lomonova, E.A. Efficiency of a regenerative direct-drive electromagnetic active suspension. *IEEE Trans. Veh. Technol.* **2011**, *60*, 1384–1393. [CrossRef]
23. Asadi, E.; Ribeiro, R.; Khamesee, M.B.; Khajepour, A. A new adaptive hybrid electromagnetic damper: Modelling, optimization, and experiment. *Smart Mater. Struct.* **2015**, *24*, 075003. [CrossRef]
24. Boglietti, A.; Cavagnino, A.; Staton, D.; Shanel, M.; Mueller, M.; Mejuto, C. Evolution and modern approaches for thermal analysis of electrical machines. *IEEE Trans. Ind. Electron.* **2009**, *56*, 871–882. [CrossRef]
25. Gysen, B.L.; Janssen, J.L.; Paulides, J.J.; Lomonova, E.A. Design aspects of an active electromagnetic suspension system for automotive applications. *IEEE Trans. Ind. Appl.* **2009**, *45*, 1589–1597. [CrossRef]
26. Wang, J.; Jewell, G.W.; Howe, D. A general framework for the analysis and design of tubular linear permanent magnet machines. *IEEE Trans. Magn.* **1999**, *35*, 1986–2000. [CrossRef]
27. ISO 2631-1. *Mechanical Vibration and Shock-Evaluation of Human Exposure to Whole-Body Vibration-Part 1: General Requirements*; International Organization for Standardization: Geneva, Switzerland, 1997.

28. Kim, Y.; Kwon, H.; Kim, S.; Kim, C.; Kim, T. Correlation of ride comfort evaluation methods for railway vehicles. *Proc. Inst. Mech. Eng. F J. Rail Rapid Transit* **2003**, *217*, 73–88. [CrossRef]
29. Han, C. Lifetime evaluation of class e electrical insulation for small induction motors. *IEEE Electr. Insul. Mag.* **2011**, *3*, 14–19.
30. Vese, I.-C.; Marignetti, F.; Radulescu, M.M. Multiphysics approach to numerical modeling of a permanent-magnet tubular linear motor. *IEEE Trans. Ind. Electron.* **2010**, *57*, 320–326. [CrossRef]
31. Bracikowski, N.; Hecquet, M.; Brochet, P.; Shirinskii, S.V. Multiphysics modeling of a permanent magnet synchronous machine by using lumped models. *IEEE Trans. Ind. Electron.* **2012**, *59*, 2426–2437. [CrossRef]
32. Encica, L.; Paulides, J.J.; Lomonova, E.A.; Vandenput, A.J. Electromagnetic and thermal design of a linear actuator using output polynomial space mapping. *IEEE Trans. Ind. Appl.* **2008**, *44*, 534–542. [CrossRef]
33. Oh, S.Y.; Cho, S.-Y.; Han, J.-H.; Lee, H.J.; Ryu, G.-H.; Kang, D.; Lee, J. Design of IPMSM rotor shape for magnet eddy-current loss reduction. *IEEE Trans. Magn.* **2014**, *50*, 841–844. [CrossRef]
34. Grauers, A.; Kasinathan, P. Force density limits in low-speed PM machines due to temperature and reactance. *IEEE Trans. Energy Convers.* **2004**, *19*, 518–525. [CrossRef]
35. Wang, J.; Howe, D. Tubular modular permanent-magnet machines equipped with quasi-halbach magnetized magnets-part I: Magnetic field distribution, EMF, and thrust force. *IEEE Trans. Magn.* **2005**, *41*, 2470–2478. [CrossRef]
36. Eckert, P.R.; Flores Filho, A.F.; Perondi, E.; Ferri, J.; Goltz, E. Design methodology of a dual-halbach array linear actuator with thermal-electromagnetic coupling. *Sensors* **2016**, *16*, 360. [CrossRef] [PubMed]
37. González-Palomino, G.; Rivas-Conde, J.; Laniado, E. Optimization of permanent magnet skew in permanent magnet linear synchronous motors using finite element and statistical method. *Engineering* **2011**, *3*, 577. [CrossRef]
38. Ashabani, M.; Mohamed, Y.A.-R.I.; Milimonfared, J. Optimum design of tubular permanent-magnet motors for thrust characteristics improvement by combined taguchi–neural network approach. *IEEE Trans. Magn.* **2010**, *46*, 4092–4100. [CrossRef]
39. Xuzhen, H.; Jiaxi, L.; Chengming, Z.; Liyi, L. Calculation and experimental study on temperature rise of a high overload tubular permanent magnet linear motor. *IEEE Trans. Plasma Sci.* **2013**, *41*, 1182–1187. [CrossRef]